

1 Short hydrogen bonds enhance non-aromatic protein-related fluorescence

2Amberley D. Stephens,*¹ Muhammad Nawaz Qaisrani,*^{2,3,4} Michael T. Ruggiero,^{5,1} Gonzalo
3Diaz Miron,⁶ Uriel N. Morzan,² Mariano C. González Lebrero,⁶ Saul T.E. Jones⁷, Emiliano
4Poli,² Andrew D. Bond,⁸ Philippa J. Woodhams,¹ Elyse M. Kleist,⁹ Luca Grisanti,¹⁰ Ralph
5Gebauer,² J. Axel Zeitler,¹ Dan Credgington,⁷ Ali Hassanali,^{2#} Gabriele S. Kaminski
6Schierle^{1#}

7

8

9¹ Chemical Engineering and Biotechnology, University of Cambridge, Cambridge CB3 0AS, UK
10² The Abdus Salam International Centre for Theoretical Physics, Strada Costiera 11, 34151 Trieste,
11 Italy
12³ SISSA International School for Advanced Studies, Via Bonomea 265, 34136 Trieste, Italy
13⁴ Institut für Physik, Johannes Gutenberg Universität, Staudingerweg 7, 55128-Mainz, Germany
14⁵ Department of Chemistry, University of Vermont, 82 University Place, Burlington, VT, 05405 USA
15⁶ Departamento de Química Inorgánica, Analítica y Química Física, INQUIMAE, Facultad de
16 Ciencias Exactas y Naturales, Universidad de Buenos Aires, Primer Piso Pabellon 2, C1428EHA,
17 Ciudad Universitaria, Argentina.
18⁷ Cavendish Laboratory, University of Cambridge, JJ Thomson Avenue, Cambridge, CB3 0HE, U.K
19⁸ Department of Chemistry, University of Cambridge, Lensfield Road, Cambridge CB2 1EW, United
20 Kingdom
21⁹ Department of Chemistry, Syracuse University, Syracuse, New York 13244, United States
22¹⁰ Division of Theoretical Physics, Ruđer Bošković Institute, Bijenička cesta 54, 10000 Zagreb,
23 Croatia
24* Contributed equally
25# Corresponding authors: ahassana@ictp.it, gsk20@cam.ac.uk
26

27

28 Abstract

29 Fluorescence in biological systems is usually associated with the presence of aromatic
30 groups. Here, we show that specific hydrogen bonding networks can significantly affect
31 fluorescence employing a combined experimental and computational approach. In particular,
32 we reveal that the single amino acid L-glutamine, by undergoing a chemical transformation
33 leading to the formation of a short hydrogen bond, displays optical properties that are
34 significantly enhanced compared to L-glutamine itself. *Ab initio* molecular dynamics
35 simulations highlight that these short hydrogen bonds prevent the appearance of a conical
36 intersection between the excited and the ground states and thereby significantly decrease non-
37 radiative transition probabilities. Our findings open the doors for the design of new
38 photoactive materials with biophotonic applications.

39

40

41

42

43Significance statement

44Intrinsic fluorescence of non-aromatic amino acids is a puzzling phenomenon with an
45enormous potential for technological and biomedical applications. The physical origins of
46this effect, however, remain elusive. Herein, we demonstrate how specific hydrogen bond
47networks can modulate fluorescence. We highlight the key role played by short hydrogen
48bonds in the networks on the ensuing fluorescence and we provide a detailed molecular
49mechanism to explain this unusual non-aromatic optical properties. Our findings should
50benefit the design of novel optically active biomaterials for applications in biosensing and
51imaging.

52

53Introduction

54

55Short peptides void of any aromatic residues have been shown to display an intrinsic
56fluorescence in the visible range (1, 2). This has primarily been observed in fibrillar protein
57structures linked to neurodegenerative diseases, such as Alzheimer's, Parkinson's and
58Huntington's diseases (3–6). Furthermore, optical properties of double amino acid based
59nanowires have also been reported, consisting either of two non-aromatic or two aromatic
60amino acids (2, 7, 8). We have previously suggested that the fluorescence of non-aromatic
61short crystal structures forming part of the amyloid-beta protein is enhanced by proton
62delocalisation (5). We have hypothesised that one of the prerequisites for this fluorescence
63observed in either amyloid structures or short peptide nanowires is related to hydrogen
64bonding or aromatic interlocks which, for the latter, decreases the bandgaps down to the
65semiconductive regions (9).

66

67Despite our previous suggestion that proton delocalisation is strongly coupled to this intrinsic
68fluorescence, its direct role on putative fluorescing states has not been elucidated. We have
69thus searched for a model system, such as a single amino acid-based structure, that displays
70similar optical properties to amyloid fibrils and is permissive to more sophisticated
71computational approaches. We have been inspired by the small peptide nanostructures that
72have been pioneered by the Gazit laboratory (9) and by the fact that there are several
73neurodegenerative diseases that have been connected with an increased level of glutamines
74produced as part of a protein, as for example Huntingtin in Huntington's disease which
75renders the protein more aggregation prone (10). It has been known that the amide group in

76L-glutamine (L-glu) is highly labile and thus can rapidly hydrolyse. We show here that the
77single amino acid L-glu upon heating in water can form a nanostructural material with optical
78properties similar to the ones observed in other amyloid fibrils such as in fibrils of amyloid-
79beta, alpha-synuclein or tau (4, 11, 12).

80

81Using X-ray diffraction (XRD), we show that L-glu dissolved in water and upon heating
82becomes cyclised forming a previously unreported structure which resembles L-
83pyroglutamine and which has been reported to be a component of amyloid-beta in the brain
84(13), but involves a low-barrier hydrogen bonded anionic dimer with an ammonium
85counterion. We have termed the new structure, i.e. L-pyroglutamine complexed with an
86ammonium ion, L-pyro-amm. L-pyro-amm has a microcrystalline plate morphology as shown
87by scanning electron microscopy (SEM). The newly formed solid has a unique hydrogen
88bond network formed by very strong hydrogen bonds (SHB) with a length of approximately
892.45 Å which is confirmed by using terahertz time-domain spectroscopy (THz-TDS).

90

91By employing a combination of electronic structure calculations and *ab initio* molecular
92dynamics in the ground and excited state we provide an interpretation of the reported
93experiments. We illustrate the important contribution of different vibrational distortions on
94the optical properties. Furthermore, our simulations identify the origins of the non-aromatic
95fluorescence in L-pyro-amm, demonstrating the key role played by the SHBs, which prevent
96the appearance of a conical intersection, significantly reducing the chances of non-radiative
97relaxation towards the ground state and hence increasing the optical properties.

98

99Methods and Materials

100

101Experimental

102Sample preparation of L-glutamine

103L-glutamine (L-glu) (#G3126, #G8540, Sigma-Aldrich, Gillingham, UK) and L-
104pyroglutamine (L-pyro) (#83160, Sigma-Aldrich) were dissolved in 18.2Ω MilliQ H₂O at a
105concentration of 0.3 M or 1 M. Aliquots were placed in a 65°C oven, since heating up
106proteins to 65°C increases the formation of amyloid structures as reported previously (14).
107Each aliquot was rotated to dissolve the powder once a day. Samples were either analysed in
108liquid form or dried on a glass or quartz cover slip (#043210.KG, Alfa Aesar, Lancashire,

109UK) either at room temperature (RT) or on a heat block set to 50°C. L-pyro-amm formed
110translucent crystals when dried.

111

112*Emission and excitation wavelength scans*

113Emission and excitation spectra were taken on a Hitachi F-4500 FL spectrophotometer
114(Hitachi High-Technologies Corporation, Tokyo, Japan) at room temperature (RT) in a quartz
115cuvette. For measurements, the excitation slit resolution was 5 nm or 10 nm and the emission
116slit resolution was 20 nm. The PMT voltage was set at 950 V and the scan speed set at 240
117nm/min. The excitation scan was measured between 250 – 400 nm and the emission filter set
118to the emission maxima of the sample stated in the figure legend, with a slit resolution of 20
119nm. The emission scan was measured between 380 - 560 nm and the excitation filter set to
120the excitation maxima of the sample stated in the figure legend, using a slit resolution of 5
121nm. Four measurements were taken for each sample which were repeated at least three times
122and the background (air or H₂O) was subtracted from the average.

123

124*Absorption measurements*

125Absorption measurements were taken on a UV-Vis-NIR Spectrophotometer, UV-3600 Plus
126(Shimadzu, Kyoto, Japan) and Cary 6000i (Agilent, Santa Clara, USA). 1 M or 0.3 M L-glu,
127L-pyro or L-pyro-amm solutions were measured in 10 mm QX cuvettes (Hellma Analytics,
128Müllheim, Germany) or dried on quartz coverslips. Measurements were taken between
129wavelengths 200 – 800 nm using 1 nm steps at a slow scan speed and a 1 nm resolution. The
130light source change wavelength was set at 393 nm and the grating change wavelength set at
131750 nm. Both direct and integrating sphere measurements were taken and showed little
132difference in results, direct measurements are shown in the manuscript. Samples were
133measured at least three times and the experiments repeated at least three times, measurements
134were then averaged and H₂O or coverslip only control was subtracted.

135

136*SEM (scanning electron microscopy)*

137SEM was performed using a FEI Magellan 400 HR-SEM at an acceleration voltage of 2 kV.
138L-pyro-amm samples were lyophilised by freezing in liquid nitrogen and freeze drying in a
139LyoQuest 85 (Telstar, Terrassa, Spain) and imaged on a glass coverslip.

140

141*X-ray diffraction*

142L-pyro-amm was dried on a glass coverslip in a 50°C oven and then at RT until crystals
143formed. Single crystal X-ray diffraction (SCXRD) measurements were performed at 180 °K
144with a Bruker D8-QUEST PHOTON-100 diffractometer, which utilised a Cu K α radiation (λ
145= 1.54 Å), and an APEX-II CCD. Absorption corrections were made using SDABS, and data
146integration and reduction were performed with SAINT+. All non-hydrogen atoms were
147refined isotropically and anisotropically, followed by inclusion of the hydrogen atoms
148(determined using the excess electron density) and refinement isotropically. The structure is
149deposited in The Cambridge Crystallographic Data Centre, CCDC No. 1981551.

150

151*Terahertz Time-Domain Spectroscopy*

152All THz-TDS spectra were acquired using a commercial Terapulse 4000 spectrometer
153(TeraView Ltd, Cambridge, UK). Samples were prepared for THz-TDS measurements by
154diluting the solid air dried L-pyro-amm with polyethylene (~ 10% w/w concentration) by
155gentle mixing using an agate mortar, followed by pressing into 2 mm thick, 13 mm diameter
156pellets using a hydraulic press. All THz-TDS spectra shown are a result of division of sample
157and blank datasets, with the blank dataset represented the THz-TDS response of a pellet of
158pure polyethylene.

159

160*Theoretical*

161*Density functional theory (DFT)-THz Calculations*

162Calculations were performed using both the CRYSTAL17 (15) and Quantum Espresso (16)
163software packages. Geometry optimisations and vibrational analyses performed with the
164CRYSTAL17 code utilised the atom-centred split-valence triple-zeta 6-311g(2d,2p) basis set
165for all atom types. Based on a previous study related to ionic molecular crystals (17), the
166range-corrected WB97-X (18) functional was used. The vibrational analysis was performed
167within harmonic approximation, and infrared intensities were determined using the Berry
168Phase method (19). Energy convergence criteria were set to $\Delta E < 10^{-8}$ and 10^{-11} hartree for the
169geometry and frequency calculations, respectively.

170

171*Periodic time dependent (TD)-Density Functional Theory (DFT) Excited State Calculations*

172Simulations were performed using the fully periodic Quantum Espresso software package.
173The Becke-Lee-Yang-Parr (B3LYP) hybrid density functional was used with an energy
174cutoff of 40 Ry. The calculations of the excited state were performed within the framework of
175TDDFT using the Liouville-Lanczos formalism implemented in the freely available

Quantum-Espresso package (20). In this approach, the optical spectra are obtained directly over the wide spectral range without taking into account the numerically complex calculations of the single excited states. We used plane wave basis set and the electron-ion interactions were taken into account via norm conserving Martins-Troullier pseudopotentials (21). To determine the ground state wave function, we used the gamma point of the Brillouin zone. All the periodic calculations employed the computationally demanding B3LYP (22) hybrid functional, the kinetic energy cutoff of 40 Ry was used for the wave functions. The intrinsic band width for the spectra was set to 0.003 Ry (~0.0408 eV).

184

185 *Periodic Structure Geometry Optimisation*

The structures obtained from the experiments were first geometrically optimized at 0°K using the Broyden-Fletcher-Goldfarb-Shanno (BFGS) minimisation algorithm implemented in CP2K (23, 24) package. A convergence criterion for the wave function optimisation was used as 5×10^{-7} a.u.. Applying the method of the Gaussian and plane wave, the wave function was expanded in the Gaussian double-zeta valence polarised (DZVP) basis set. The cutoff for the electronic density was set to 300 Ry. We used the gradient correction to the local density approximation and the core electrons were treated via Goedecker-Teter-Hutter pseudopotentials (25). In all the calculations, we used the Becke-Lee-Yang-Parr (BLYP) (26) functional with the D3(0) Grimme (27) dispersion corrections for the van der Waals interactions.

196

197 *Ab Initio Molecular Dynamics Simulations*

Ab initio Molecular Dynamics simulations (AIMD) were performed using Quickstep algorithm implemented in CP2K. In these calculations, the propagation of the nuclei was taken into account within the framework of the Born-Oppenheimer approximation. The simulations were performed in the NVT ensemble and the temperature was controlled during the simulations by using the velocity-rescaling thermostat (28). We used the time step of 0.5 femtosecond to update the nuclear coordinates and velocities while the total length of the simulations for each system is 50 picoseconds.

205

206 *Excited State Cluster Calculations*

A set of excited state calculations were performed on glutamine clusters in order to understand the role of the environment on the optical properties. Specifically, the optical

properties of L-pyro-amm were investigated using various isolated cluster models with the Gaussian09 software package. The clusters were extracted directly from the crystal structure and used in various combinations (dimers, trimers, tetramers) to perform TD-DFT calculations. A split-valence triple-zeta 6-311g(2d,2p) basis set was used for all atom types together with the hybrid B3LYP functional. Some benchmark simulations, comparing the optical properties obtained from the periodic calculations using B3LYP to range corrected hybrid functionals like CAM-B3LYP, were also performed with these clusters.

216

We also performed a series of excited state optimisations on various model systems built from L-pyro-amm in order to examine the nature of the geometrical distortions that occur on the lowest electronic excited state. These calculations were also performed with the Gaussian09 software package. All clusters were surrounded with a continuum dielectric constant of 80, representing pure H₂O. The 6-311G(2d,2p) basis set was used for all atoms together with the range corrected hybrid functional CAM-B3LYP (29). The clusters were first optimised in the ground state after which they were optimised on the first electronic excited state.

225

Non-adiabatic Decay Probabilities Using Excited State Molecular Dynamics

Excited state AIMD was employed, as implemented in the LIO quantum-chemical package (<https://github.com/MALBECC/lio>) (30–33), to analyse the influence of three key factors determining the optical properties of L-pyro-amm: (i) the formation of a SHB, (ii) the presence of ammonium, and (iii) the combination of ring deplanarisation and carbonyl stretching. Our model system for this study was the L-pyro-amm dimer with a single SHB. In order to assess the influence of the ammonium ion on the optical properties of L-pyro-amm, AIMD was performed both on the L-pyro-amm with and without the ammonium ion. Analogously, in order to shed light on the role of the SHB in the L-pyro-amm fluorescence, in addition to performing simulations of L-pyro at the natural SHB distance of 2.5 Å, we performed three replicas constraining the HB distance to 3.0 Å, 3.5 Å and 4.5 Å, respectively.

237

The initial structures for this analysis were extracted from the ground state AIMD described above. Subsequently, 3 ps ground state AIMD at 300K was performed to equilibrate the system, followed by 1ps of excited state AIMD. The non-radiative decay probability (NRP) was computed every time step using the TDDFT-based Trajectory Surface Hopping algorithm without permitting decays to the ground state (34–36). The non-adiabatic coupling

elements between $S0$ and $S1$ (Equation 1) can be estimated analytically employing the method introduced by Tapavicza, *et al.*, (37).

$$\sigma_{S0,S1} = \langle \Psi_{S0}(r, R(t)) | \nabla_R | \Psi_{S1}(r, R(t)) \rangle \quad (1)$$

In this context, the non-radiative decay probability (NRP) from $S1$ to $S0$ (Equation 2) is expressed as:

$$NRP(t) = -2 \int_t^{t+\Delta t} dt' \frac{Re[C_{S1}C_{S0}^* \sigma_{S0,S1}(t')]}{C_{S0}C_{S0}^*}, \quad (2)$$

where C coefficients satisfy (Equation 3)

$$i\hbar \frac{\partial C_i(t)}{\partial t} = C_i(t)\omega_i - i\hbar \sum_{j=0}^{N_{states}} C_j \sigma_{ij}. \quad (3)$$

NRP(t) is the probability for the system to relax from $S1$ to $S0$ without fluorescent emission at time t . Hence, the accumulated non-radiative decay probability (Equation 4) accounts for the total relaxation probability from the excitation instant ($t=0$) up to time t .

$$ANRP(t) = \int_0^t dt' NRP(t') \quad (4)$$

As mentioned above, this methodology was applied to five different initial conditions of the dimer at SHB, 3.0, 3.5, and 4.5 Å of hydrogen distance and for the dimer-amm at SHB distance. In order to avoid introducing large structural deformations, the distance constraints in the HB were introduced in combination with position restrains on the nitrogen and the C_β of the pyroglutamic ring.

The excited state AIMDs were performed employing the density functional theory (DFT) using the hybrid functional PBE0 level (38), with a 6-31G basis set and a time step of 0.5 fs. The computation of excitation energies, excited-state gradients, and non-adiabatic coupling vectors, the Linear Response TDDFT method was used within the Tamm-Dancoff approximation (37, 39).

Results and Discussion

It has long been known that poly-glutamine can form amyloid-like fibrillar structures *in vitro*. The more glutamine residues in the poly-glutamine polymer, the faster the aggregation propensity of the polypeptide chain. This led us to investigate whether L-glu on its own, under conditions which normally promote fibril formation, such as an increase in temperature

274(14), was able to form structures with similar optical properties, as recently observed for
275amyloid fibrils (5, 40, 41).

276

277We first investigated the structure of L-pyro-amm, which formed after incubation of L-glu for
2788 days at 65°C, using SEM and observed crystal structures shown in Fig. 1a. However, in
279order to investigate whether L-glu had indeed changed its crystal structure arrangement we
280performed XRD analysis of the resulting material. In Fig. 1b we show the crystal structure of
281the heated L-glu structure, which we termed L-pyro-amm, and the published crystal
282structures of L-glu and L-pyroglutamine (L-pyro) in Suppl. Fig. 1. Note, the L-pyro structure
283was analysed as it displayed structural similarities to the newly formed L-pyro-amm. Figures
284were obtained from geometry optimisations of the nuclear positions of the atoms using
285experimental densities. L-pyro-amm consists of 8 pyroglutamine groups and 4 ammonium
286ions (144 atoms) complexed within the crystal (see Fig. 1b). In contrast, as shown in Suppl.
287Fig. 1a, L-glu consists of 4 glutamine molecules (80 atoms) in the unit cell which form
288hydrogen bonds involving the termini and side chain. Furthermore, as shown in Suppl. Fig.
2891b, L-pyro consists of 12 pyroglutamine molecules (192 atoms) in the unit cell forming
290hydrogen bonds involving the NH and COOH groups.

291

292L-pyro-amm has a rather unique hydrogen bond network structure since four of the
293pyroglutamine molecules are deprotonated and hence have a nominal negative charge, while
294the other four molecules are neutral. One of the important implications of this difference is
295that L-pyro-amm contains a very strong hydrogen bond. The red circled regions in Fig. 1b
296correspond to a short hydrogen bonds (SHBs) with a length of 2.45 Å, while those in L-glu
297and L-pyro range between ~2.55-2.85 Å, Suppl. Fig. 1.

298

299The structural change was further confirmed using THz-TDS measurements, as this technique
300is strongly dependent on the bulk packing arrangement as well as on the internal covalent
301structure of the molecules (42). The THz-TDS spectrum of the resulting solid, as well as the
302solid-state DFT predicted spectrum based on the single crystal XRD (SCXRD)-determined
303structure, is shown in Fig. 1c (full spectral assignment available in Suppl. Fig. 2). The
304agreement between the experimental and theoretical spectra further supports that full
305conversion of the sample occurs and thus enables additional investigations into the structural
306and electronic properties of the material. The agreement is also indicative of the ability of the

theoretical model to not only reproduce the experimental structure, but also the weak forces found in solid structures.

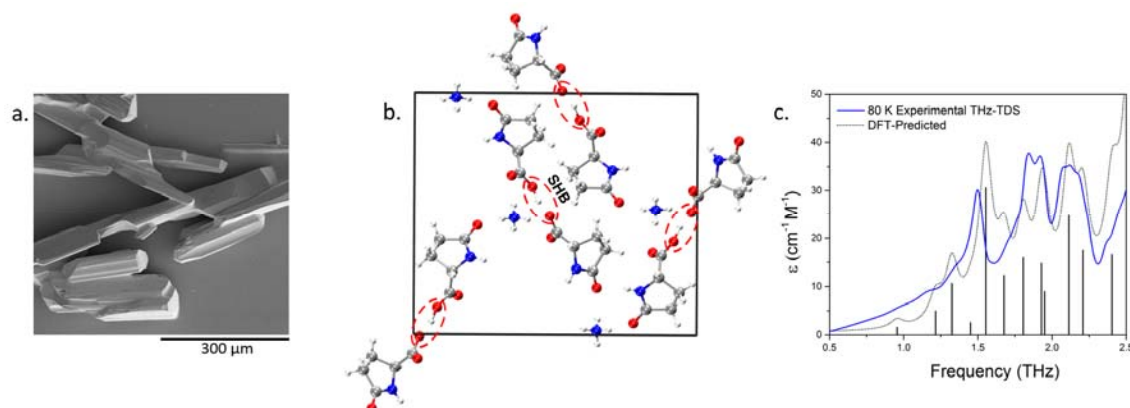


Figure 1. L-glu forms L-pyro-amm upon heating.

(a) SEM image of crystals of L-pyro-amm dried. (b) XRD analysis of heated L-glu sample show the newly formed structure, L-pyro-amm. Geometry optimisations show that 8 pyroglutamine groups and four ammonium ions (144 atoms) are complexed in the crystal and a SHB of 2.45 Å (within red dashed lines) is present near the ammonium ion (white-hydrogen, red-oxygen, blue-nitrogen, grey-carbon). (c) Experimental (blue line) and theoretical (grey line) THz-TDS of the L-pyro-amm sample are in agreement and confirm the presence of the new L-pyro-amm structure.

We first investigated whether there were any differences in the optical properties associated with the three crystal structures. Comparing the absorption of L-glu, L-pyro and L-pyro-amm in water, we show that only L-pyro-amm has a significantly red-shifted absorption which lies in the 275-320 nm range, whereas both L-glu and L-pyro primarily absorb in the deep UV (<250 nm) (see Fig. 2a).

We next compared the experimental absorption spectra of L-glu, L-pyro and L-pyro-amm with the ones obtained from time dependent density functional theory (TDDFT). We highlight here, that the small size of the systems permitted us to determine the spectra using a hybrid functional, thereby not only advancing the quality of our theoretical predictions from previous studies (5, 40, 41) but also coupling the optical properties directly to different vibrational modes.

Fig. 2b illustrates the absorption spectra obtained for the TDDFT calculations on the 3 periodic systems in the ground state (i.e. at 0 °K). Panel b.i) shows the relative oscillator strength as a function of the frequency while panel b.ii) illustrates the second derivative of the oscillator strength permitting the positions of the maxima in the spectra to be more easily identified. The spectra reveal some striking differences between the different systems. Interestingly, we observe that L-pyro is essentially dark throughout the frequency range up to ~ 6eV. On the other hand, L-pyro-amm shows the presence of more structure in the spectrum. Specifically, it is the only system for which the spectrum features a low energy excitation at 226 nm (5.5 eV) and subsequently other peaks slightly above 220 nm (5.625eV) and 216 nm (5.75eV). While L-glu exhibits a peak at 222 nm (5.58eV), it is dark up to 206 nm (~6eV).

342

We have previously shown that thermal fluctuations and in particular nuclear vibrations, such as proton transfer, have a large impact on the absorption spectra of peptide structures as compared to the 0 °K behavior (5, 43–45). In Fig. 2c we show that, compared to the 0 °K spectra in Fig. 2b, thermal fluctuations cause a large red shift to around 3.4 eV (365 nm) for L-pyro-amm, close to what is observed experimentally. These spectra were computed averaging over 25 frames sampled from the molecular dynamics simulations. Interestingly, no such effect is observed for L-glu which remains weakly absorbing up to more than 5 eV (247 nm) as seen at 0 °K.

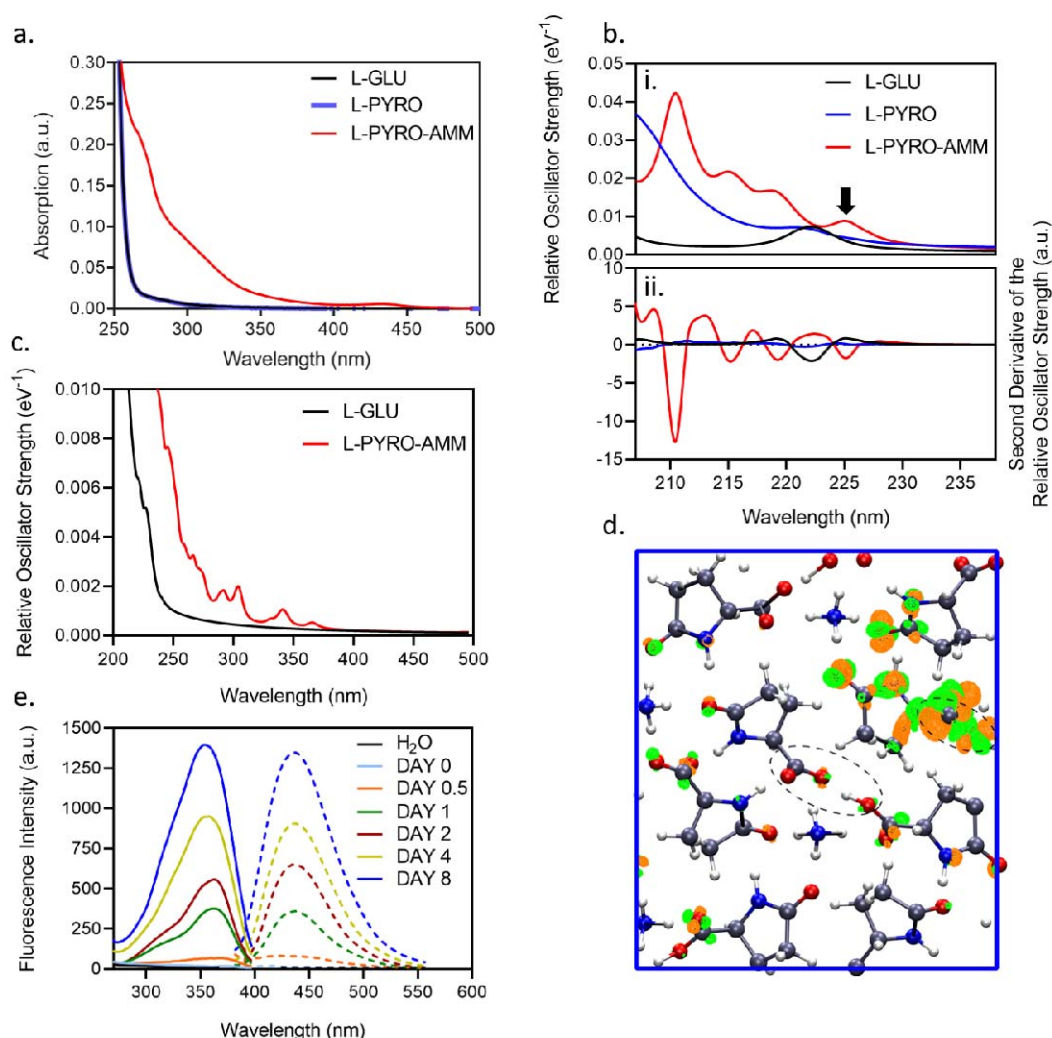
351

In order to understand better the physical origin of the low energy excitation at 226 nm (~5.5 eV) in L-pyro-amm, we computed the electron response density at this frequency. This is illustrated in Fig. 2d, where we observe that most of the electron response is localised in regions around the pyroglutamine rings as well as regions near the SHB (see dashed circle in Fig. 2d). The optical response thus entails a charge reorganisation involving several parts of the molecular crystal. However, since L-pyro contains the same pyroglutamine rings as L-pyro-amm but absorbs more in the UV-spectrum, we conclude that the structural changes in the crystal in the presence of the SHB, which are the main features that distinguish L-pyro from L-pyro-amm, are responsible for the large Stokes shift observed in L-pyro experimentally and computationally.

362

We next investigated whether the above structures also display fluorescence excitation and emission properties as has been observed for amyloid-like structures reported previously (5,

36540, 41). Fig. 2e shows the excitation scan from 250-400 nm (solid lines) with the emission set
366at 430 nm of L-glu in water at day 0 to 8 after incubation at 65°C. We observe an excitation
367peak at around 360 nm which is similar to what we have measured previously for amyloid
368proteins (5). The corresponding emission scan (dashed lines) with the excitation set at 360
369nm and emission from 380-560 nm showed an emission peak around 430 nm, again lying in
370the same visible range as for amyloid fibrils. When the L-pyro-amm solution was dried the
371excitation and emission peaks were slightly blue shifted (Suppl. Fig. 3a) which may be due to
372a change in the molecular environment in the dried state. Importantly, we do not see any
373fluorescence in L-glu (without heating, i.e. at day 0 Fig. 2e.). To determine the importance of
374the ammonium ion experimentally, L-pyro was incubated in water and heated at 65°C for 8
375days, and only a very weak fluorescence has been detected (Suppl. Fig. 3b).

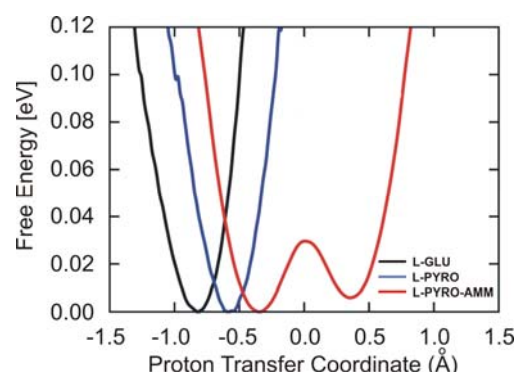


376
377**Figure 2. Optical properties of L-pyro-amm are distinct from L-glu and L-pyro.**

(a) Absorption spectra of 0.3 M L-glu (black), L-pyro (blue) and L-pyro-amm (red) (L-glu incubated for 8 days at 65°C) in water taken between 200 – 500 nm shows primarily features of L-pyro-amm. (b) Absorption spectra of L-glu, L-pyro and L-pyro-amm obtained from periodic density functional theory calculations with the B3LYP functional. L-pyro-amm features the lowest lying excited states which are characterised by the largest oscillator strengths. (c) Absorption spectra for L-glu and L-pyro-amm obtained from periodic simulations at room temperature. The spectra were computed by averaging over 25 frames randomly sampled from the *ab initio* molecular dynamics simulations. (d) The excited state electron density computed for L-pyro-amm from the optimised structure computed at the first peak (arrow in panel b). The lowest excited state density shows a response from various parts of the crystal structure including the pyroglutamic acid ring and the SHB region (see dashed circle). The orange and green surfaces correspond to regions involving a decrease and increase in electron density respectively, shown at an iso-value of 1×10^{-5} . (e) 1 M L-glu was incubated at 65°C and the excitation and emission spectra were measured over time. Excitation spectra were measured between 250-400 nm with emission set at 420 nm and emission spectra were measured between 380-560 nm with the excitation set at 360 nm.

394

As alluded to earlier, one of the factors that distinguishes L-pyro-amm from the other systems is the presence of the SHB (highlighted by red circles in Fig. 1b) and the presence of the ammonium ion. In order to characterise the behaviour of the SHB, we conducted *ab initio* molecular dynamics simulations of the three systems at 300 °K and examined the proton transfer coordinates defined as the difference in distance between the proton (H) and the two oxygen atoms (O1 and O2) that sandwich it and is commonly referred to as the proton transfer coordinate ($d_{O1-H} - d_{O2-H}$) as shown in Fig. 3 for different types of hydrogen bonds in the crystals. It is clear that the SHB in L-pyro-amm is characterised by a double-well potential. The barrier associated with this proton transfer is on the order of thermal energy, indicating that zero-point energy (ZPE) would make the proton transfer barrierless (46). An examination of similar proton transfer coordinates for hydrogen bonds in L-glu and L-pyro show that they are characterised by only single-well potentials.



407

408

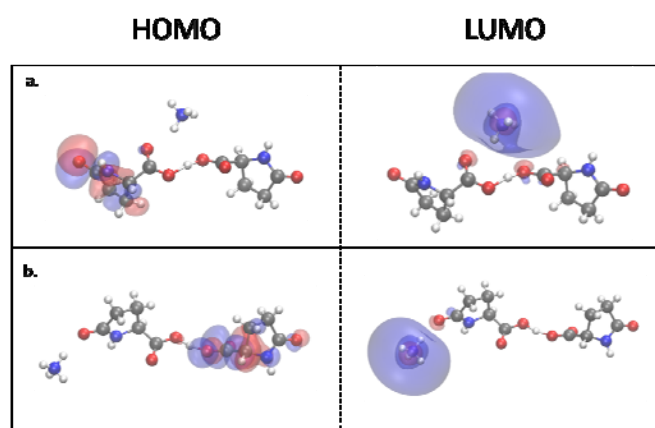
409 **Figure 3: Free energy profiles along the proton transfer coordinate show only L-pyro-**
 410 **amm displays a double well potential.** Free energy profiles along the proton transfer
 411 coordinate are displayed for L-glu (black), L-pyro (blue) and L-pyro-amm (red) at room
 412 temperature. The L-glu and L-pyro display single well potentials, while the L-pyro-amm
 413 system is the only one the exhibits a double well potential implying that there is proton
 414 transfer from one side to the other.

415

416 The nature of the optical properties is sensitive to the environment in which the glutamine
 417 molecules reside. It has previously been reported that charged amino acids already display an
 418 absorption in the range of 250-350 nm that is significantly red shifted (47, 48). The origins of
 419 the low energy absorption were attributed to charge transfer excitations. The simulations of
 420 these systems were performed in the gas phase, rather than considering the protein
 421 environment such as shown for L-pyro-amm in Fig 2d. In comparison to the results presented
 422 in Fig. 2d, data presented in Fig. 4, show that the origins of the electronic transitions equally
 423 arise from a charge transfer (CT) between the highest occupied molecular orbital (HOMO) on
 424 the anionic dimer, and the lowest unoccupied molecular orbital (LUMO) centred on the
 425 ammonium cation when performed in the gas phase. Interestingly, the correct transition
 426 energy is only predicted when the ammonium cation is spatially near the centre of the dimer,
 427 which corresponds to the delocalisation of the negative charge and the SHB. Two generalised
 428 geometries, with the ammonium cation near the SHB (as seen in Fig. 4a) and away from the
 429 SHB (Fig. 4b), with the corresponding HOMO and LUMO orbitals are shown. The results
 430 predict a transition of 304 nm for dimer (a) and 669 nm for dimer (b), with dimer (a) most
 431 closely resembling the chemical environment present within the crystalline material.

432

The results show that charge transfer is capable to lead to absorption in the near UV when investigated in the gas phase, i.e. neglecting the direct protein environment. However, including the protein environment in the molecular crystal (Fig. 2d) results instead in the excitation being a charge reorganisation involving several different molecular groups of the crystal. Indeed, by shuffling the protons along the SHBs in the ground-state, we observe an electronic response involving the entire structural units of L-pyro-amm including both the hydrogen bonded regions and the pyroglutamic acid rings when the protein environment is accounted for (Suppl. Fig. 4).



441

Figure 4. Comparison of the HOMO and LUMO orbitals on two L-pyro-amm models.

L-pyro-amm structures are presented where the ammonium cation is located directly near the hydrogen bond (a), and where the ammonium cation is located away from the hydrogen bond (b). While both models predicted charge-transfer HOMO-LUMO states, only in the case of (a) is the transition predicted to be in the vicinity of the experimentally observed peak, 304 nm compared to 669 nm for (b).

448

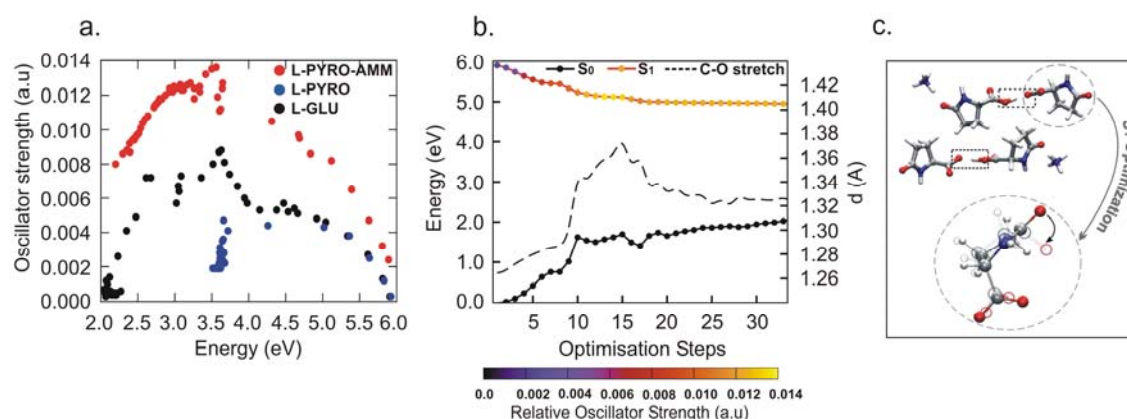
Up to this point, we have shown that proton transfer along SHBs is an important part of the structural fluctuations in the ground state structure of L-pyro-amm. In order to characterise the nuclear relaxation upon photoexcitation, we conducted both excited state optimisations as well as excited state molecular dynamics simulations. We first show the results from the excited state optimisations obtained from clusters carved out from the different glutamine crystals and surrounded by a continuum dielectric constant of 80. Fig. 5a shows a scatter plot of the difference between the first excited state and ground-state energies as well as the corresponding oscillator strengths for the three systems, L-glu, L-pyro and L-pyro-amm. The scatter plots were obtained over the course of the excited state optimisation. We observe that

the L-pyro-amm system is characterised by the largest oscillator strengths peaking at approximately 3.5 eV (354 nm), which is consistent with our experimental findings. Although L-glu and L-pyro also have a peak at around 3.5 eV it is much weaker than the one of L-pyro-amm. We thus decided to focus on a series of excited state optimisations for various clusters of L-pyro-amm.

463

Fig. 5b shows the evolution of the first excited state energy for one of the L-pyro-amm clusters (Fig. 5c) across the optimisation steps. We find that the excited state energy drops by 0.5 eV combined with an enhancement of the oscillator strength while the ground state energy, shown in solid-black, rises by about 1.5 eV. In this case, the closing of the energy gap to approximately 3 eV is associated with an increase of the carbonyl oxygen bond as observed in previous studies (48–50), as well as a de-planarisation of the pyroglutamine ring (see Fig. 5c). Similar features are also observed in other clusters including one with the ammonium ion closer to the short hydrogen bond (Suppl. Fig. 5).

472



473

Figure 5. L-pyro-amm optical properties as seen through excited state optimisations.

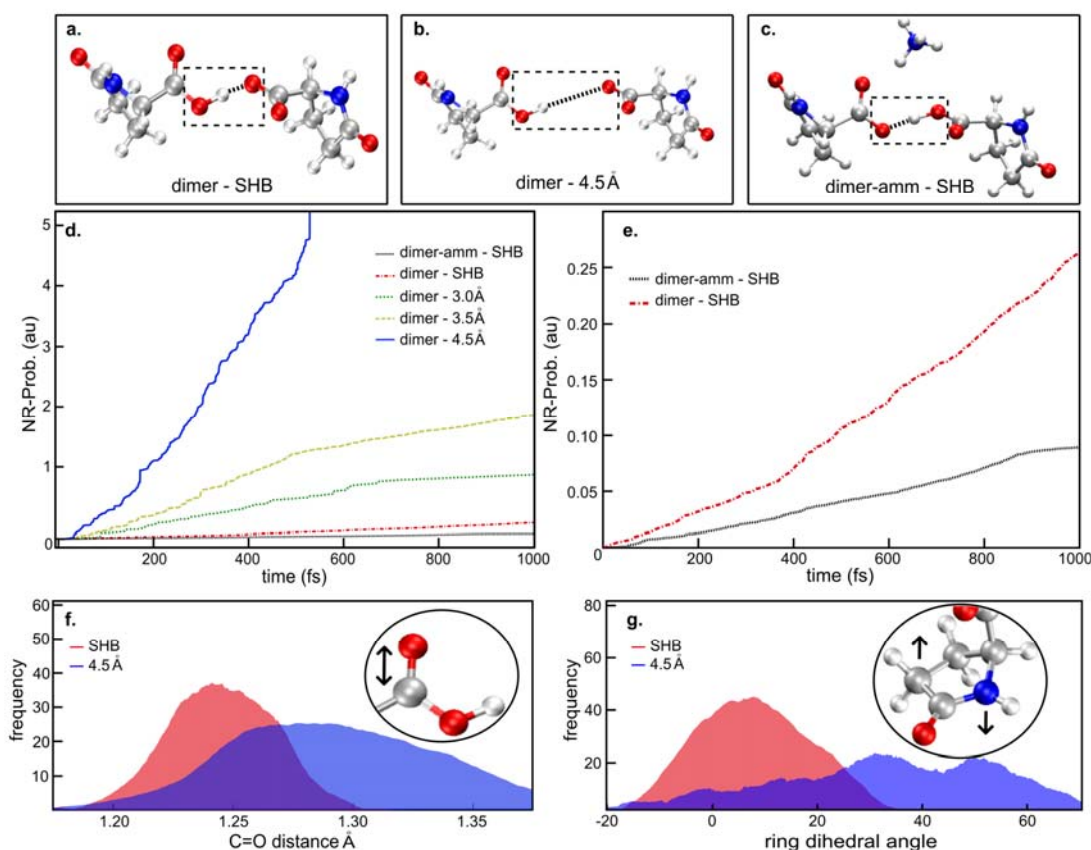
(a) Scatter plot of the oscillator strengths versus the emission energy (defined as the difference between the first excited state and the ground-state) during the excited state optimisations of L-glu (black), L-pyro (blue) and L-pyro-amm (red). (b) Ground and excited state energies are plotted as a function of the excited state optimisation of the system shown in c. The curves on the excited state are colour-coded with the oscillator strengths. S₀ and S₁ refer to the ground and excited state energies, respectively. (c) A snapshot of the optimised excited state cluster also showing the lengthening of the carbonyl bond and the deplanarisation of the ring.

483

To further explore the preceding mechanisms, we next turn to deploying non-adiabatic decay estimations using excited state ab initio molecular dynamics simulations, as implemented in the LIO quantum-chemical package (<https://github.com/MALBECC/lio>) (30–33). This approach enables investigating the $S_0 \leftarrow S_1$ de-excitation probability providing a clear interpretation of the ensuing optical properties of L-pyro-amm (see Methods for details). The nature of the $S_0 \leftarrow S_1$ transition is mainly a $v''=0 \leftarrow v'=0$ (where v' and v'' are the vibrational quantum numbers in the electronic ground and excited state respectively) with a FC factor between ground vibrational levels of ~ 0.82 (see Suppl. Fig. 6), therefore the excited state simulation was initiated by a vertical excitation to the S_1 state. We performed two sets of excited state simulations: (i) varying the strength of the SHB to study its influence on the fluorescence of L-pyro dimer (Fig.6 a-b), and (ii) comparing L-pyro with L-pyro-amm dimers, to assess the role of ammonium ion on the transient excited state dynamics (Fig. 6c). Each trajectory was propagated for 1 ps from which the non-radiative decay probability (NRP) was determined by the fewest-switches trajectory surface hopping approach (34–36). Fig. 6d shows the time evolution of the accumulated NRP for various hydrogen bond lengths. The accumulated NRP (ANRP) represents the total probability for $S_0 \leftarrow S_1$ non-radiative relaxation. The larger value of the NRP implies that the system has a higher likelihood of decaying non-radiatively to the ground-state. On the other hand, a lower NRP would involve a longer excited-state lifetime increasing the fluorescence probability. Fig. 6d demonstrates unequivocally that the presence of the short hydrogen bond significantly reduces the chances of non-radiative relaxation towards the ground state. Examining the energy gap between the excited and ground state for this system shows that it occurs approximately ~ 3 eV (413 nm) (see Suppl. Fig. 7a) consistent with fluorescence in the blue/green visible regime. The presence of the ammonium ion further enhances, albeit by a subtle amount, the probability of trapping the system in the excited state.

509

510



511

512 **Figure 6. Excited state AIMD highlight how the presence of a SHB and the ammonium**
 513 **ion is enhancing fluorescence.** Excited state AIMD performed for the (a) L-pyro dimer, (b)
 514 the L-pyro dimer constraining the SHB distance, and (c) the L-pyro-amm. (d) Accumulated
 515 non-radiative $S_0 \leftarrow S_1$ decay probability (ANRP) for L-pyro dimer (dimer-SHB) and the
 516 constrained SHB L-pyro (dimer-) where the SHB distance was fixed at 3.0 Å, 3.5 Å and 4.5
 517 Å and for the L-pyro-amm dimer (dimer-amm-SHB). (e.) Accumulated non-radiative decay
 518 probability for L-pyro (red discontinuous line) and L-pyro-amm (black dashed line). (f)
 519 Carboxyl C=O distance histogram for the L-pyro-amm dimer at the SHB distance (red curve)
 520 or constraining the SHB bond to 4.5 Å (blue curve). (g) Ring dihedral angle histogram for the
 521 L-pyro-amm dimer at the SHB distance (red curve) or constraining the SHB bond to 4.5 Å
 522 (blue curve).

523

524 The excited state optimisations shown in Fig. 5, illustrate the important role played by the
 525 vibrational distortions in the excited state that on the ensuing optical property. In agreement
 526 with this, Figs. 6f and g show the distribution of the C=O bond length and the ring de-
 527 planarisation (computed as the sum of its internal dihedral angles) for the dimer systems with

the SHB and weaker (longer) hydrogen bonds in the left and right panel, respectively. Interestingly, we see that the trajectories that undergo non-radiative decay are characterised by both, a significant increase in the carbonyl stretch (C=O bond length) by about a tenth of an Angstrom, and a large de-planarisation of the dihedral angle. The combined distortion of these vibrational coordinates leads to non-radiative decay as observed in the dimer system with longer hydrogen bonds. In the system with the short and strong hydrogen bonds, these modes are hampered which essentially prevents the system from easily accessing conical intersections. This increases the likelihood of observing fluorescence in the L-pyro-amm structure characterised by short-hydrogen-bonds. Therefore, both our experiments and simulations demonstrate the crucial role played by the SHB and in determining the fluorescence of L-pyro-amm.

Conclusions

The experimental and theoretical findings presented here, elucidate a rather complex molecular mechanism associated with the non-aromatic intrinsic fluorescence in protein-like structures. In the case of L-glutamine, a chemical reaction creates a newly formed structure involving a cyclised pyroglutamic acid ring. This new structure features absorption in the UV and emission in the visible range very similar to the chemically distinct amyloid fibrils (4, 5, 11, 12, 49–51). The structural chromophore responsible for the optical properties in this new protein-related structure arises from a hydrogen bond network associated with structures involving short hydrogen bonds. Indeed, we have shown previously that similar to L-pyro-amm, the crystallised structure of the hydrophobic core of amyloid beta, 2Y3J, L-pyro-amm contains a SHB (52) leading to a double well potential in the ground state. The presence of strong hydrogen bonds along which proton transfer occurs and secondly, specific ionic interactions in close proximity, such as involving the ammonium ion of L-pyro-amm, affect the optical properties. Although the fluorescence observed in these systems is much weaker compared to conventional fluorophores, the physical and chemical properties of the hydrogen bond networks reported here maybe a generic feature across many other peptide structures.

Our non-adiabatic molecular dynamics simulations demonstrate that the presence of short hydrogen bonds with specific environmental conditions hinder vibrational deformations that can access conical intersections, as was previously speculated (5). The role of carbonyl groups is also consistent with a recent experimental study showing their importance for non-

aromatic fluorescence (53). SHBs have recently been observed in different biological systems which have long been associated with either intrinsic fluorescence, such as NADP/NAD (54), FAD/FMN (55), the light-sensing chromophore in photoactive yellow protein (56), or in the active site of many enzymes, such as hydrolases and oxidoreductases (57, 58), many of which consist of a highly complex H-bond structures similar to amyloid proteins. Furthermore, it has been recently reported that 1 in every 16 hydrogen bonds in over 1600 proteins are characterised by short hydrogen bonds (58). Thus, the mechanisms we espouse here may be more general. Our findings offer the possibility of designing novel biomaterial for applications in optical sensing or the design of novel biocompatible catalysts.

571

Supporting Information

Supporting data include; Supplementary Figure 1. Clusters of L-glu and L-pyro. Supplementary Figure 2. Full spectral assignment of THz data. Supplementary Figure 3. L-pyro-amm has blue shifted fluorescence when dried and displays higher fluorescence intensity than L-pyro. Supplementary Figure 4. The optical properties of L-pyro-amm are sensitive to the environment and involves the electronic response of the entire structure. Supplementary Figure 5. L-pyro-amm undergoes vibrational distortions upon excitation as seen through excited state optimisations. Supplementary Figure 6. Potential energy surface along the SHB proton transfer coordinate in the ground (S₀, panels A and D) and the excited (S₁, panels B and C) states. Supplementary Figure 7. The energy gap between excited and ground state of L-pyro-amm is consistent with the experiments and eventually deactivates via a conical intersection back to the ground state. SCXRD data are available at the Cambridge Crystallographic Data Centre, CCDC No. 1981551. Raw data are available at the University of Cambridge Repository <https://doi.org/10.17863/CAM.57945>.

586

Author Information

Corresponding Authors

Ali A. Hassanali, ahassana@ictp.it

Gabriele S. Kaminski Schierle, gsk20@cam.ac.uk

591

Author Contributions

G.S.K.S and A.H conceptualised the manuscript. *A.D.S and M.N.Q contributed equally. A.D.S prepared samples for all experimental data. P.J.W. performed SEM experiments. A.D.B and M.T.R performed XRD measurements. M.T.R. performed THz experiments and

596DFT-THz calculations. A.D.S. performed excitation and emission measurements. A.D.S and
597S.T.J. performed absorption measurements. M.T.R and E.M.K performed TD-DFT cluster
598calculations. M.N.Q, E.P, L.G, R.G and A.H performed AIMD, Periodic TD-DFT Excited
599State Calculations and Periodic Structure Geometry Optimisation calculations. G.D.M,
600U.N.M, and M.C.GL performed excited state molecular dynamics. A.D.S, M.N.Q, M.T.R,
601S.T.J, L.G, G.D.M, U.N.M, M.C.G.L, J.A.Z, D.C, A.H and G.S.K.S contributed to
602manuscript writing. All authors have given approval to the final version of the manuscript.

603

604Notes

605The authors declare no competing financial interest.

606

607Acknowledgments

608We thank Bluebell Drummond, Talia Shmool and Chetan Poudel for work that is not in the
609final manuscript.

610

611Funding Sources

612G.S.KS. acknowledges funding from the Wellcome Trust (065807/Z/01/Z) (203249/Z/16/Z),
613the UK Medical Research Council (MRC) (MR/K02292X/1), Alzheimer Research UK
614(ARUK) (ARUK-PG013-14), Michael J Fox Foundation (16238) and Infinitus China Ltd.
615M.T.R and J.A.Z acknowledge EPSRC funding (EP/N022769/1). P.J.W acknowledges
616EPSRC funding (EP/L016087/1). A.D.S. acknowledges Alzheimer Research UK the British
617Biophysical Society (BSS) for travel grants.

618

619Abbreviations

620SEM, scanning electron microscopy; XRD, X-ray diffraction; THz-TDS, terahertz time
621domain spectroscopy; DFT, density functional theory; TD-DFT, time dependent DFT; SHB,
622short hydrogen bond; CT, charge transfer; L-glu, L-glutamine; L-pyro, L-pyroglutamine; L-
623pyro-amm, L-pyroglutamine complexed with an ammonium ion.

624

625References:

6261. A. Shukla, S. Mukherjee, S. Sharma, V. Agrawal, K. V. R. Kishan, P. Guptasarma, A
627 novel UV laser-induced visible blue radiation from protein crystals and aggregates:
628 Scattering artifacts or fluorescence transitions of peptide electrons delocalized through
629 hydrogen bonding? *Arch. Biochem. Biophys.* **428**, 144–153 (2004).

6302. G. Rosenman, N. Amdursky, M. Molotskii, D. Aronov, L. Adler-Abramovich, E.
631 Gazit, Blue luminescence based on quantum confinement at peptide nanotubes. *Nano*
632 *Lett.* **9**, 3111–3115 (2009).
6333. F. T. Chan, D. Pinotsi, G. S. K. Schierle, C. F. Kaminski, in *Bio-nanoimaging: Protein*
634 *Misfolding and Aggregation* (Elsevier, 2013;
635 <http://linkinghub.elsevier.com/retrieve/pii/B9780123944313000134>), pp. 147–155.
6364. F. T. S. Chan, G. S. Kaminski Schierle, J. R. Kumita, C. W. Bertoncini, C. M. Dobson,
637 C. F. Kaminski, C. V Robinson, C. M. Dobson, J. Beard, P. Das, K. Jansen, M.
638 DeLucia, W.-L. Lin, G. Dolios, R. Wang, C. B. Eckman, D. W. Dickson, M. Hutton, J.
639 Hardy, T. Golde, Protein amyloids develop an intrinsic fluorescence signature during
640 aggregation. *Analyst.* **138**, 2156 (2013).
6415. D. Pinotsi, L. Grisanti, P. Mahou, R. Gebauer, C. F. Kaminski, A. Hassanali, G. S.
642 Kaminski Schierle, Proton Transfer and Structure-Specific Fluorescence in Hydrogen
643 Bond-Rich Protein Structures. *J. Am. Chem. Soc.* **138**, 3046–3057 (2016).
6446. J. Pansieri, V. Jossierand, S. J. Lee, A. Rongier, D. Imbert, M. M. Sallanon, E. Kövari,
645 T. G. Dane, C. Vendrely, O. Chaix-Pluchery, M. Guidetti, J. Vollaie, A. Fertin, Y.
646 Usson, P. Rannou, J. L. Coll, C. Marquette, V. Forge, Ultraviolet–visible–near-infrared
647 optical properties of amyloid fibrils shed light on amyloidogenesis. *Nat. Photonics.* **13**,
648 473–479 (2019).
6497. L. Adler-Abramovich, E. Gazit, The physical properties of supramolecular peptide
650 assemblies: From building block association to technological applications. *Chem. Soc.*
651 *Rev.* **43**, 7236–7236 (2014).
6528. L. Adler-Abramovich, M. Reches, V. L. Sedman, S. Allen, S. J. B. Tendler, E. Gazit,
653 Thermal and chemical stability of diphenylalanine peptide nanotubes: Implications for
654 nanotechnological applications. *Langmuir.* **22**, 1313–1320 (2006).
6559. K. Tao, P. Makam, R. Aizen, E. Gazit, Self-assembling peptide semiconductors.
656 *Science (80-.).* **358** (2017), p. eaam9756.
65710. J. M. Andresen, J. Gayán, L. Djoussé, S. Roberts, D. Brocklebank, S. S. Cherny, L. R.
658 Cardon, J. F. Gusella, M. E. Macdonald, R. H. Myers, D. E. Housman, N. S. Wexler, J.
659 Lorimer, J. Porter, F. Gomez, C. Moskowitz, K. P. Gerstenhaber, E. Shackell, K.
660 Marder, G. Penchaszadeh, S. A. Roberts, A. Brickman, D. Brocklebank, J. Gray, S. R.
661 Dlouhy, S. Wiktorski, M. E. Hodes, P. M. Conneally, J. B. Penney, J. F. Gusella, J. H.
662 Cha, M. Irizarry, D. Rosas, S. Hersch, Z. Hollingsworth, A. B. Young, D. E. Housman,
663 M. M. de Young, E. Bonilla, T. Stillings, A. Negrette, S. R. Snodgrass, M. D.

664 Martinez-Jaurrieta, M. A. Ramos-Arroyoh, J. Bickham, J. S. Ramos, F. Marshall, I.
665 Shoulson, G. J. Rey, A. Feigin, N. Arnheim, A. Acevedo-Cruz, L. Acosta, J. Alvir, K.
666 Fischbeck, L. M. Thompson, A. Young, L. Dure, C. J. O'Brien, J. Paulsen, S. P.
667 Moran, D. Krch, P. Hogarth, D. S. Higgins, B. Landwehrmeyer, M. R. Hayden, E. W.
668 Almqvist, R. R. Brinkman, O. Suchowersky, A. Durr, C. C. Dodé, F. Squitieri, P. J.
669 Morrison, M. Nance, C. A. Ross, R. L. Margolis, A. Rosenblatt, G. T. Estrella, D. M.
670 Cabrero, R. J. A. Trent, E. McCusker, A. Novelletto, M. Frontali, J. S. Paulsen, R.
671 Jones, A. Zanko, T. Ashizawa, A. Lazzarini, J. L. Li, V. C. Wheeler, A. L. Russ, G.
672 Xu, J. S. Mysore, T. Gillis, M. Hakky, L. A. Cupples, M. Saint-Hilaire, S. M. Hersch,
673 The relationship between CAG repeat length and age of onset differs for Huntington's
674 disease patients with juvenile onset or adult onset. *Ann. Hum. Genet.* **71**, 295–301
675 (2007).

67611. D. Pinotsi, A. K. Buell, C. M. Dobson, G. S. Kaminski Schierle, C. F. Kaminski, A
677 Label-Free, Quantitative Assay of Amyloid Fibril Growth Based on Intrinsic
678 Fluorescence. *ChemBioChem.* **14**, 846–850 (2013).

67912. T. N. Tikhonova, N. R. Rovnyagina, A. Y. Zhrebker, N. N. Sluchanko, A. A.
680 Rubekina, A. S. Orekhov, E. N. Nikolaev, V. V. Fadeev, V. N. Uversky, E. A.
681 Shirshin, Dissection of the deep-blue autofluorescence changes accompanying amyloid
682 fibrillation. *Arch. Biochem. Biophys.* **651**, 13–20 (2018).

68313. H. Mori, K. Takio, M. Ogawara, D. J. Selkoe, Mass spectrometry of purified amyloid
684 β protein in Alzheimer's disease. *J. Biol. Chem.* **267**, 17082–17086 (1992).

68514. M. Fändrich, C. M. Dobson, The behaviour of polyamino acids reveals an inverse side
686 chain effect in amyloid structure formation. *EMBO J.* **21**, 5682–90 (2002).

68715. R. Dovesi, A. Erba, R. Orlando, C. M. Zicovich-Wilson, B. Civalleri, L. Maschio, M.
688 Rérat, S. Casassa, J. Baima, S. Salustro, B. Kirtman, Quantum-mechanical condensed
689 matter simulations with CRYSTAL. *Wiley Interdiscip. Rev. Comput. Mol. Sci.* **8**,
690 e1360 (2018).

69116. P. Giannozzi, O. Andreussi, T. Brumme, O. Bunau, M. Buongiorno Nardelli, M.
692 Calandra, R. Car, C. Cavazzoni, D. Ceresoli, M. Cococcioni, N. Colonna, I. Carnimeo,
693 A. Dal Corso, S. De Gironcoli, P. Delugas, R. A. Distasio, A. Ferretti, A. Floris, G.
694 Fratesi, G. Fugallo, R. Gebauer, U. Gerstmann, F. Giustino, T. Gorni, J. Jia, M.
695 Kawamura, H. Y. Ko, A. Kokalj, E. Küçükbenli, M. Lazzeri, M. Marsili, N. Marzari,
696 F. Mauri, N. L. Nguyen, H. V. Nguyen, A. Otero-De-La-Roza, L. Paulatto, S. Poncé,
697 D. Rocca, R. Sabatini, B. Santra, M. Schlipf, A. P. Seitsonen, A. Smogunov, I.

- 698 Timrov, T. Thonhauser, P. Umari, N. Vast, X. Wu, S. Baroni, Advanced capabilities
699 for materials modelling with Quantum ESPRESSO. *J. Phys. Condens. Matter.* **29**
700 (2017), doi:10.1088/1361-648X/aa8f79.
70117. M. T. Ruggiero, J. Gooch, J. Zubieta, T. M. Korter, Evaluation of Range-Corrected
702 Density Functionals for the Simulation of Pyridinium-Containing Molecular Crystals.
703 *J. Phys. Chem. A.* **120**, 939–947 (2016).
70418. J. Da Chai, M. Head-Gordon, Long-range corrected hybrid density functionals with
705 damped atom-atom dispersion corrections. *Phys. Chem. Chem. Phys.* **10**, 6615–6620
706 (2008).
70719. Y. Noel, C. M. Zicovich-Wilson, B. Civalieri, P. D’Arco, R. Dovesi, Polarization
708 properties of ZnO and BeO: An ab initio study through the Berry phase and Wannier
709 functions approaches. *Phys. Rev. B - Condens. Matter Mater. Phys.* **65**, 1–9 (2002).
71020. D. Rocca, R. Gebauer, Y. Saad, S. Baroni, Turbo charging time-dependent density-
711 functional theory with Lanczos chains. *J. Chem. Phys.* **128** (2008),
712 doi:10.1063/1.2899649.
71321. N. Troullier, J. L. Martins, Efficient pseudopotentials for plane-wave calculations.
714 *Phys. Rev. B.* **43**, 1993–2006 (1991).
71522. A. D. Becke, Density-functional thermochemistry. III. The role of exact exchange. *J.*
716 *Chem. Phys.* **98**, 5648–5652 (1993).
71723. J. D. Head, M. C. Zerner, A Broyden-Fletcher-Goldfarb-Shanno optimization
718 procedure for molecular geometries. *Chem. Phys. Lett.* **122**, 264–270 (1985).
71924. J. VandeVondele, M. Krack, F. Mohamed, M. Parrinello, T. Chassaing, J. Hutter,
720 Quickstep: Fast and accurate density functional calculations using a mixed Gaussian
721 and plane waves approach. *Comput. Phys. Commun.* **167**, 103–128 (2005).
72225. S. Goedecker, M. Teter, Separable dual-space Gaussian pseudopotentials. *Phys. Rev. B*
723 *- Condens. Matter Mater. Phys.* **54**, 1703–1710 (1996).
72426. A. D. Becke, Density-functional exchange-energy approximation with correct
725 asymptotic behavior. *Phys. Rev. A.* **38**, 3098–3100 (1988).
72627. S. Grimme, J. Antony, S. Ehrlich, H. Krieg, A consistent and accurate *ab initio*
727 parametrization of density functional dispersion correction (DFT-D) for the 94
728 elements H-Pu. *J. Chem. Phys.* **132**, 154104 (2010).
72928. G. Bussi, D. Donadio, M. Parrinello, Canonical sampling through velocity rescaling. *J.*
730 *Chem. Phys.* **126** (2007), doi:10.1063/1.2408420.
73129. T. Yanai, D. P. Tew, N. C. Handy, A new hybrid exchange-correlation functional

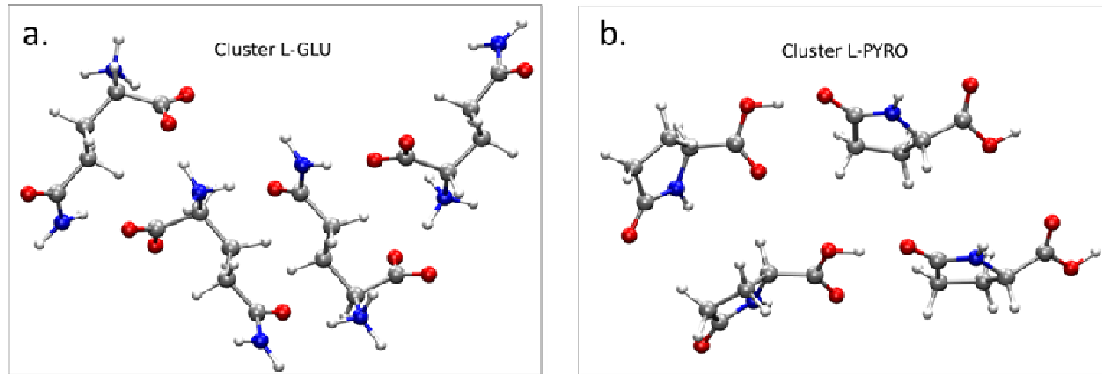
- 732 using the Coulomb-attenuating method (CAM-B3LYP). *Chem. Phys. Lett.* **393**, 51–57
- 733 (2004).
73430. J. P. Marcolongo, A. Zeida, J. A. Semelak, N. O. Foglia, U. N. Morzan, D. A. Estrin,
- 735 M. C. González Lebrero, D. A. Scherlis, Chemical Reactivity and Spectroscopy
- 736 Explored From QM/MM Molecular Dynamics Simulations Using the LIO Code.
- 737 *Front. Chem.* **6**, 70 (2018).
73831. U. N. Morzan, F. F. Ramírez, M. B. Oviedo, C. G. Sánchez, D. A. Scherlis, M. C. G.
- 739 Lebrero, Electron dynamics in complex environments with real-time time dependent
- 740 density functional theory in a QM-MM framework. *J. Chem. Phys.* **140**, 164105
- 741 (2014).
74232. M. A. Nitsche, M. Ferreria, E. E. Mocskos, M. C. G. Lebrero, GPU accelerated
- 743 implementation of density functional theory for hybrid QM/MM simulations. *J. Chem.*
- 744 *Theory Comput.* **10**, 959–967 (2014).
74533. F. Ramírez, · Gonzalo, D. Mirón, M. C. González Lebrero, D. A. Scherlis, QM-MM
- 746 Ehrenfest dynamics from first principles: photodissociation of diazine in aqueous
- 747 solution. *Theor. Chem. Acc.* **137**, 124 (2018).
74834. E. Tapavicza, I. Tavernelli, U. Rothlisberger, Trajectory surface hopping within linear
- 749 response time-dependent density-functional theory. *Phys. Rev. Lett.* **98**, 023001
- 750 (2007).
75135. J. C. Tully, Molecular dynamics with electronic transitions. *J. Chem. Phys.* **93**, 1061–
- 752 1071 (1990).
75336. M. Barbatti, Nonadiabatic dynamics with trajectory surface hopping method. *Wiley*
- 754 *Interdiscip. Rev. Comput. Mol. Sci.* **1** (2011), pp. 620–633.
75537. E. Tapavicza, G. D. Bellchambers, J. C. Vincent, F. Furche, Ab initio non-adiabatic
- 756 molecular dynamics. *Phys. Chem. Chem. Phys.* **15** (2013), pp. 18336–18348.
75738. C. Adamo, V. Barone, Toward reliable density functional methods without adjustable
- 758 parameters: The PBE0 model. *J. Chem. Phys.* **110**, 6158–6170 (1999).
75939. S. Hirata, M. Head-Gordon, Time-dependent density functional theory within the
- 760 Tamm-Dancoff approximation. *Chem. Phys. Lett.* **314**, 291–299 (1999).
76140. K. Jong, Y. Taghipour Azar, L. Grisanti, A. D. Stephens, S. T. E. Jones, D.
- 762 Credgington, G. S. Kaminski Schierle, A. A. Hassanali, Low Energy Optical
- 763 Excitations as an Indicator of Structural Changes Initiated at the Termini of Amyloid
- 764 Protein. *Phys. Chem. Chem. Phys.* (2019), doi:10.1039/c9cp04648h.
76541. L. Grisanti, D. Pinotsi, R. Gebauer, G. S. Kaminski Schierle, A. A. Hassanali, A

- 766 computational study on how structure influences the optical properties in model crystal
767 structures of amyloid fibrils. *Phys. Chem. Chem. Phys.* **19**, 4030–4040 (2017).
76842. E. P. J. Parrott, J. A. Zeitler, Terahertz time-domain and low-frequency Raman
769 spectroscopy of organic materials. *Appl. Spectrosc.* **69**, 1–25 (2015).
77043. Y. K. Law, A. A. Hassanali, Role of Quantum Vibrations on the Structural, Electronic,
771 and Optical Properties of 9-Methylguanine. *J. Phys. Chem. A.* **119**, 10816–10827
772 (2015).
77344. S. Sappati, A. Hassanali, R. Gebauer, P. Ghosh, Nuclear quantum effects in a
774 HIV/cancer inhibitor: The case of ellipticine. *J. Chem. Phys.* **145** (2016),
775 doi:10.1063/1.4968046.
77645. Y. K. Law, A. A. Hassanali, The importance of nuclear quantum effects in spectral line
777 broadening of optical spectra and electrostatic properties in aromatic chromophores. *J.*
778 *Chem. Phys.* **148** (2018), doi:10.1063/1.5005056.
77946. D. Marx, Erratum: Proton transfer 200 years after von grothuss: Insights from Ab
780 initio simulations (ChemPhysChem (2006) 7 (1848-1810)). *ChemPhysChem.* **8**, 209–
781 210 (2007).
78247. S. Prasad, I. Mandal, S. Singh, A. Paul, B. Mandal, R. Venkatramani, R. Swaminathan,
783 Near UV-Visible electronic absorption originating from charged amino acids in a
784 monomeric protein. *Chem. Sci.* **8**, 5416–5433 (2017).
78548. I. Mandal, S. Paul, R. Venkatramani, Optical backbone-sidechain charge transfer
786 transitions in proteins sensitive to secondary structure and modifications. *Faraday*
787 *Discuss.* **207**, 115–135 (2018).
78849. A. Handelman, N. Kuritz, A. Natan, G. Rosenman, Reconstructive Phase Transition in
789 Ultrashort Peptide Nanostructures and Induced Visible Photoluminescence. *Langmuir.*
790 **32** (2016), pp. 2847–2862.
79150. S. K. Joseph, N. Kuritz, E. Yahel, N. Lapshina, G. Rosenman, A. Natan, Proton-
792 Transfer-Induced Fluorescence in Self-Assembled Short Peptides. *J. Phys. Chem. A.*
793 **123**, 1758–1765 (2019).
79451. L. L. Del Mercato, P. P. Pompa, G. Maruccio, A. Della Torre, S. Sabella, A. M.
795 Tamburro, R. Cingolani, R. Rinaldi, Charge transport and intrinsic fluorescence in
796 amyloid-like fibrils. *Proc Natl Acad Sci U S A.* **104**, 18019–18024 (2007).
79752. K. Jong, L. Grisanti, A. Hassanali, Hydrogen Bond Networks and Hydrophobic Effects
798 in the Amyloid β 30-35Chain in Water: A Molecular Dynamics Study. *J. Chem. Inf.*
799 *Model.* **57**, 1548–1562 (2017).

80053. C. Niyangoda, T. Miti, L. Breydo, V. Uversky, M. Muschol, Carbonyl-based blue
801 autofluorescence of proteins and amino acids. *PLoS One*. **12**, e0176983 (2017).
80254. A. Stavrinides, E. C. Tatsis, L. Caputi, E. Foureau, C. E. M. Stevenson, D. M. Lawson,
803 V. Courdavault, S. E. O'Connor, Structural investigation of heteroyohimbine alkaloid
804 synthesis reveals active site elements that control stereoselectivity. *Nat. Commun.* **7**
805 (2016), doi:10.1038/ncomms12116.
80655. F. Forneris, D. P. H. M. Heuts, M. Delvecchio, S. Rovida, M. W. Fraaije, A. Mattevi,
807 Structural analysis of the catalytic mechanism and stereoselectivity in *Streptomyces*
808 *coelicolor* alditol oxidase. *Biochemistry*. **47**, 978–985 (2008).
80956. S. Yamaguchi, H. Kamikubo, K. Kurihara, R. Kuroki, N. Niimura, N. Shimizu, Y.
810 Yamazaki, M. Kataoka, Low-barrier hydrogen bond in photoactive yellow protein.
811 *Proc. Natl. Acad. Sci. U. S. A.* **106**, 440–444 (2009).
81257. W. W. Cleland, P. A. Frey, J. A. Gerlt, The low barrier hydrogen bond in enzymatic
813 catalysis. *J. Biol. Chem.* **273** (1998), pp. 25529–25532.
81458. S. Zhou, L. Wang, Unraveling the structural and chemical features of biological short
815 hydrogen bonds. *Chem. Sci.* **10**, 7734–7745 (2019).

816
817
818
819
820
821
822
823
824
825
826
827
828
829
830
831
832
833

834
835
836Supplementary Information for
837
838Short hydrogen bonds enhance non-aromatic protein-related fluorescence
839
840Amberley D. Stephens, Muhammad Nawaz Qaisrani, Michael T. Ruggiero, Gonzalo Diaz Miron, Uriel
841N. Morzan, Mariano C. González Lebrero, Saul T.E. Jones, Emiliano Poli, Andrew D. Bond, Philippa
842J. Woodhams, Elyse M. Kleist, Luca Grisanti, Ralph Gebauer, J. Axel Zeitler, Dan Credgington, Ali
843Hassanali, Gabriele S. Kaminski Schierle
844
845Ali Hassanali, Gabriele S. Kaminski Schierle
846Email: ahassana@ictp.it, gsk20@cam.ac.uk
847
848
849
850
851
852
853
854
855
856
857
858
859
860
861
862
863
864
865



866

867 **Supplementary Figure 1. Clusters of L-glu and L-pyro**

868 Structural representations of (a) L-glutamine (L-glu) and (b) L-pyroglutamine (L-pyro)

869 clusters from the published crystal structure.

870

871

872

873

874

875

876

877

878

879

880

881

882

883

884

885

886

887

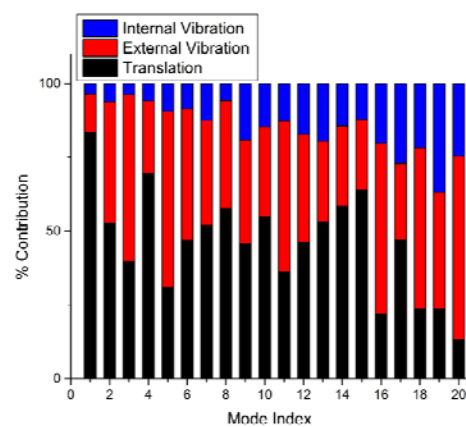
888

889

890

891

892



Mode Number	Frequency (THz)	Intensity (km mol ⁻¹)	Assignment
1	0.955	0.22	Antisymmetric translation in b
2	1.215	0.71	Coupled translation in a and rotation about bc
3	1.325	1.52	external rotation about b
4	1.450	0.36	Asymmetric translation in c
5	1.554	4.37	External rotation about a
6	1.676	1.76	Translation in a and external asymmetric rotation about H-bond coordinate
7	1.805	2.28	External asymmetric rotation of dimer pairs
8	1.929	2.11	External symmetric rotation of dimer pairs
9	1.950	1.28	Asymmetric rotation about H-bond coordinate, ammonium translational motion
10	2.113	3.53	Translation and rotation (breathing) around ammonium cation
11	2.208	2.5	Symmetric external rotation of entire formula units
12	2.404	2.87	In phase external rotation perpendicular to H-bond coordinate
13	2.502	0.45	Out of phase external rotation perpendicular to H-bond coordinate
14	2.564	0.73	External out of phase rotation of H-bonded chains about b
15	2.565	8.91	Out of phase external rotation of individual pyrroglutamic molecules with translation of ammonium cation
16	2.654	18.09	External vibration coupled with torsion of the COOH group
17	2.679	0.29	External rotation and torsion of pyrroglutamic ring
18	2.776	4.94	External rotation and torsion of ring and carbonyl group
19	2.988	2.68	External rotation and translation of ammonium

893

894Supplementary Figure 2. Full spectral assignment of THz data

895The top chart shows the contribution to each IR-active mode including external translations
896and hindered rotations, and internal vibrational motions (i.e. torsions), while the bottom table
897lists the detailed assignment for each mode.

898

899

900

901

902

903

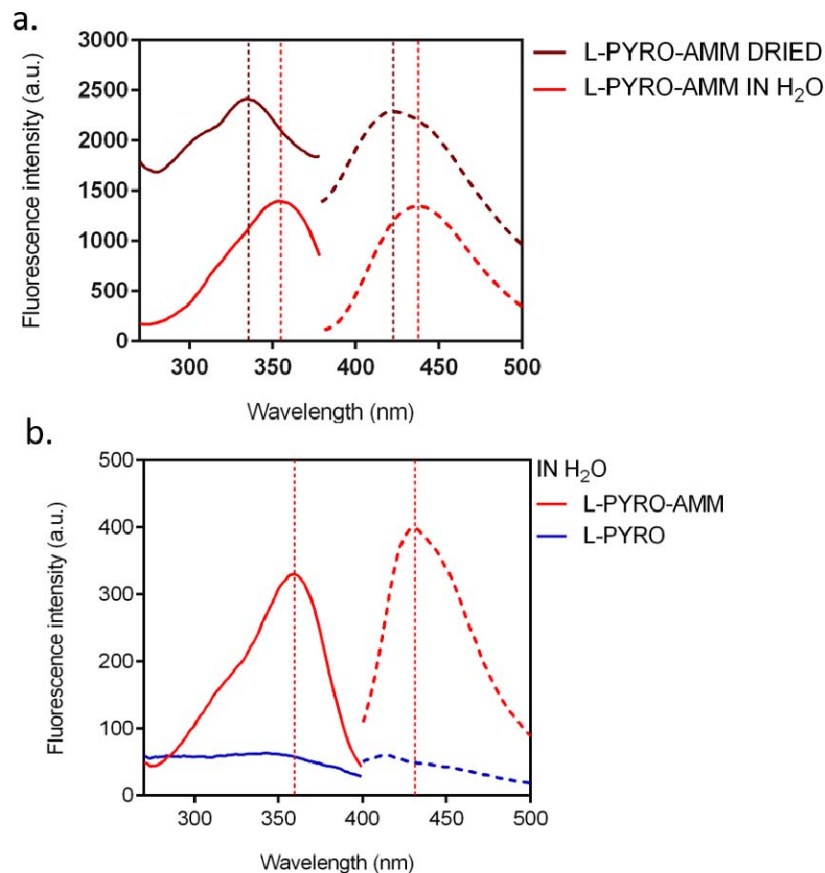
904

905

906

907

908



909

910Supplementary Figure 3. L-pyro-amm has blue shifted fluorescence when dried and
911displays higher fluorescence intensity than L-pyro

912(a)The excitation peak of L-pyro-amm when dried (solid dark red line) is blue shifted with a
 913peak maximum ~ 340 nm compared to L-pyro-amm in H₂O (solid red line) which has a peak
 914maximum ~ 360 nm. The emission peak of L-pyro-amm when dried (dashed dark red line) is
 915also blue shifted, with a peak maximum ~ 420 nm, compared to L-pyro-amm in H₂O (dashed
 916red line) with a peak maximum ~ 430 nm. (b) 1 M L-glu and 1 M L-pyro (blue) were
 917incubated in H₂O for 8 days at 65°C. After 9 days, the L-glu had converted into the L-pyro-
 918amm structure (red). L-pyro-amm has a clear excitation peak maximum at ~360 nm and
 919emission peak maximum at ~ 430 nm, while L-pyro (blue), although not completely dark, has
 920no clear excitation or emission peak.

921

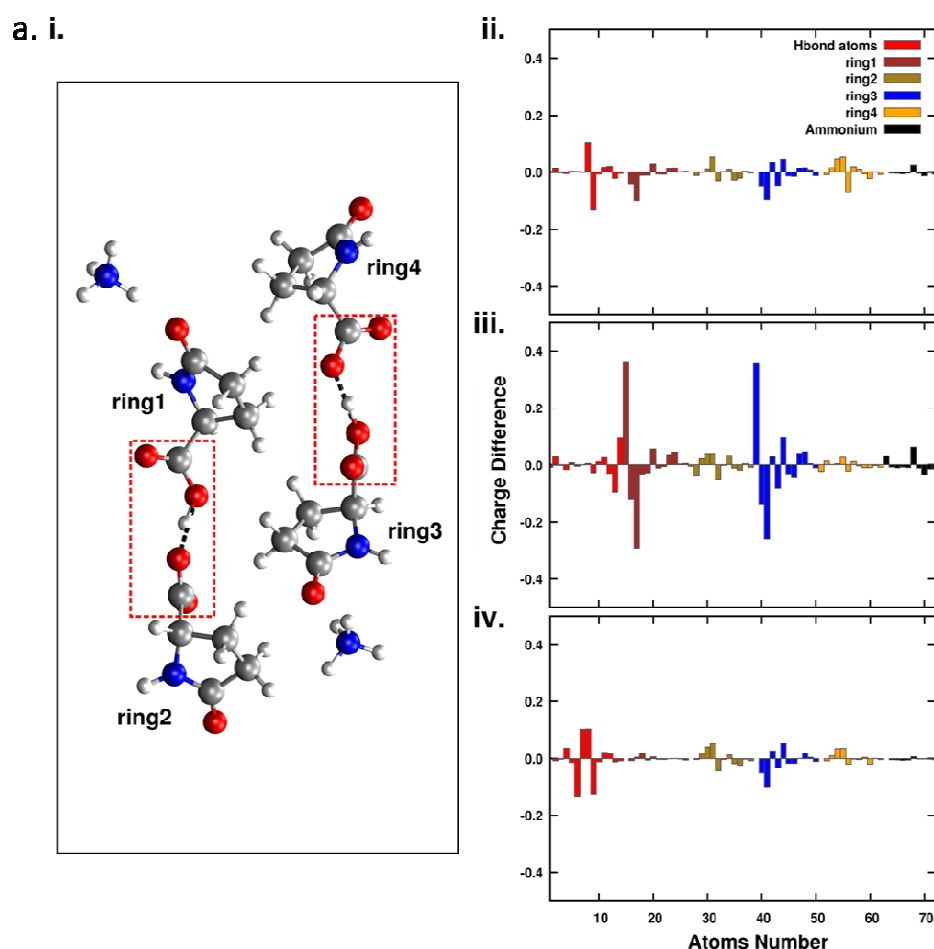
922

923

924

925

926

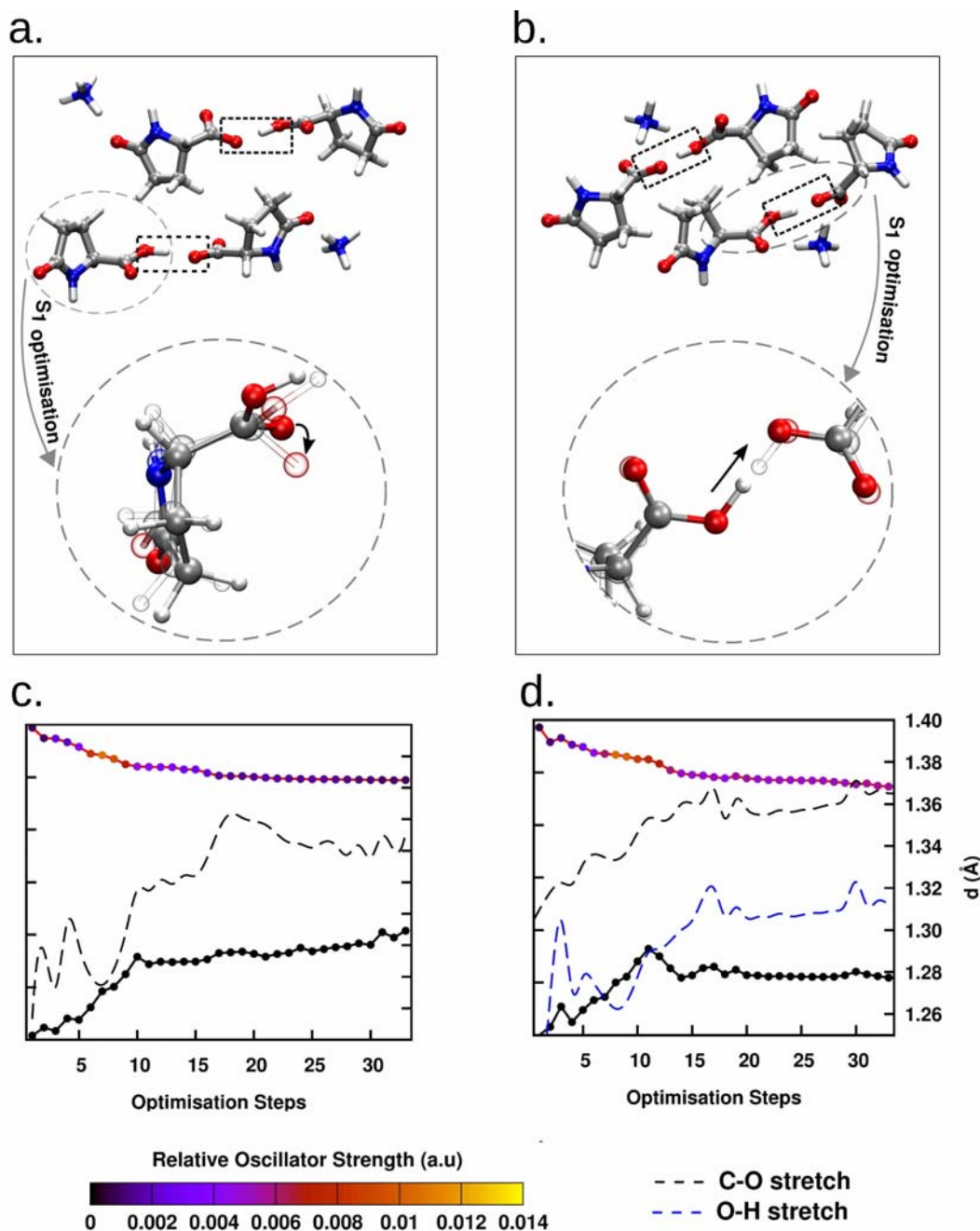


927

928 **Supplementary Figure 4. The optical properties of L-pyro-amm are sensitive to the**
 929 **environment and involves the electronic response of the entire structure**

930 (a)(i) L-pyro-amm cluster used to examine the sensitivity of the optical response on different
 931 parts of the cluster upon moving different protons. (ii) Charge differences between the ground
 932 and excited state are computed using restrained electrostatic potential atomic partial charges
 933 (RESP) for the cluster shown in i). Note, the electronic response involves all the atoms of the
 934 cluster. (iii) The two protons in the rectangle regions are displaced to be in the centre of the
 935 hydrogen bond and the charge differences are then computed. As illustrated, the proton
 936 displacement leads to a larger change in magnitude of the charges. (iv) The charge
 937 differences are computed for another nuclear configuration for which the protons are kept
 938 fixed but the O—O distance is increased from 2.45 to 3.2 Angstroms. The charge differences
 939 obtained here are quite similar to the original condition shown in (ii).

940

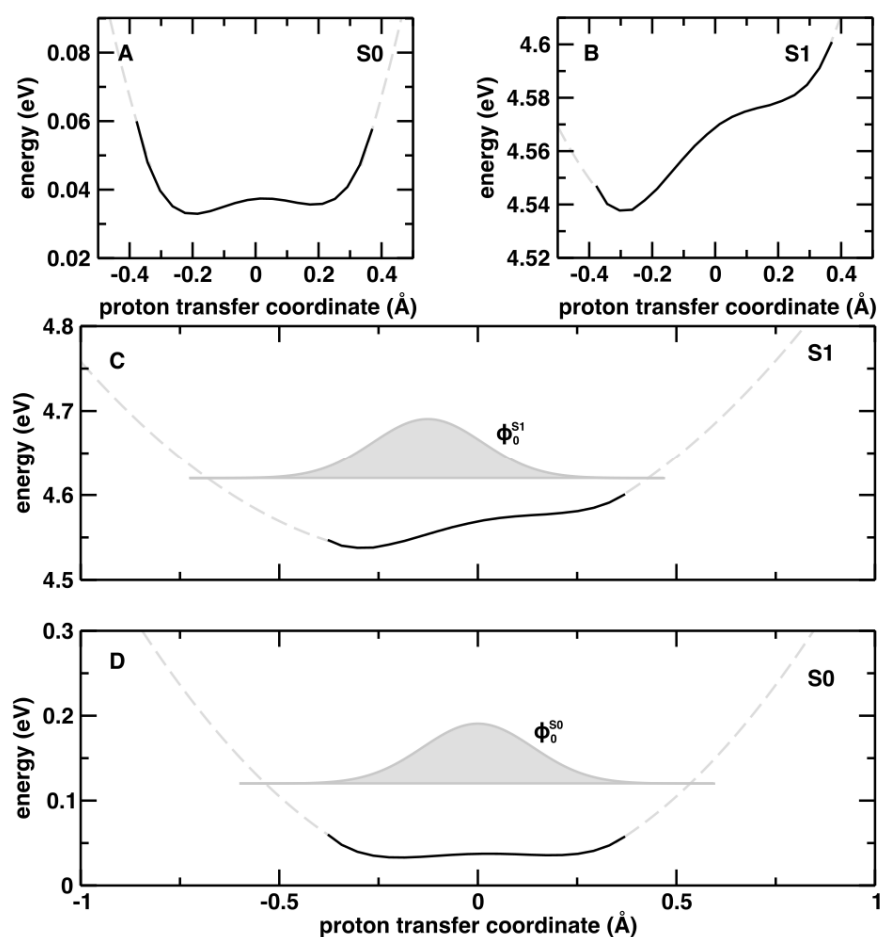


941

942 **Supplementary Figure 5. L-pyro-amm undergoes vibrational distortions upon**
 943 **excitation as seen through excited state optimisations**

944 (a-b) correspond to two additional clusters to the one reported in the main text that were built
 945 from the L-pyro-mm crystal structure. c) and (d) correspond to the evolution of the excited
 946 state energy and ground-state energy over the course of the optimisation. Also shown, are the
 947 changes in the C-O bond lengths (dashed black) which increases on the excited state surface.
 948 In (d) we show the O-H bond stretch where a proton transfer is observed on the excited state.

949



950

951

952 **Supplementary Figure 6. The S0 and S1 nuclear wavefunctions associated to the SHB**
 953 **proton transfer coordinate reveal a vibronic transition dominated by a $0 \leftarrow 0$ character.**

954 The calculated potential energy surfaces (black continuous lines) are prolonged with a
 955 quadratic fitting (gray dashed lines). Panels C and D illustrate the ground-state vibrational
 956 wavefunction in the S0 and the S1 electronic states (and respectively). The resulting
 957 Franck-Condon factor between and is 0.82, showing that the nature of the $S1 \leftarrow S0$
 958 transition is mainly a $v''=0 \leftarrow v'=0$ (where v' and v'' are the vibrational quantum numbers
 959 in the electronic ground and excited state respectively).

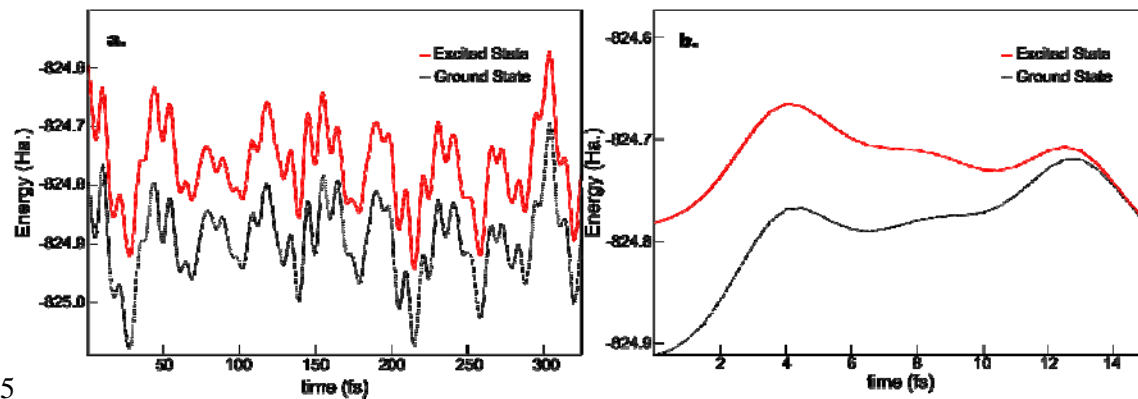
960

961

962

963

964



965

966 **Supplementary Figure 7. The energy gap between excited and ground state of L-pyro-**
 967 **amm is consistent with the experiments and eventually deactivates via a conical**
 968 **intersection back to the ground state**

969 (a) Shows the energy of the excited and ground state obtained from the excited state
 970 molecular dynamics simulations where non-adiabatic decay probabilities are estimated. We
 971 see clearly that the energy difference between the excited and ground state is approximately 3
 972 eV (413 nm) consistent with experimental data. (b) Shows the same excited state and ground
 973 state energy for another simulation where the system de-activates very quickly within 10s of
 974 femtoseconds through a conical intersection where the ground and excited state energies
 975 intersect.

976